AgriEngineering

MDPI

Article

Design and Simulation Analysis of a Bionic Weeding and Plant Protection Integrated Vehicle for Sesame

Dongdong Gu [1], Jiahan Zhang [1], Yuhan Wang [1], Xiaomei Zhang [2], Xiao Xiao [1], Jie Yang [1,*] and Huan Song [1]

[1] School of Mechanical Engineering, North China University of Water Resources and Electric Power, Zhengzhou 450046, China; wintergdd@126.com (D.G.); zhjh0115@126.com (J.Z.); wangyh0929@126.com (Y.W.); xiaoxiao@ncwu.edu.cn (X.X.); songhuan@ncwu.edu.cn (H.S.)

[2] College of Information and Management Science, Henan Agricultural University, Zhengzhou 450046, China; zhangmeihenau@126.com

* Correspondence: yangjie@ncwu.edu.cn

Abstract

To address the poor mechanical adaptability of conventional equipment to 40 cm narrow-row sesame cultivation and the high weeding resistance and energy consumption of traditional weeding tools, this study developed an integrated bionic weeding and plant protection vehicle. The vehicle features a modular structure capable of three-row weeding and four-row plant protection, coupled with an extended-range hybrid powertrain. Its parallel linkage design enables terrain adaptation, ensuring consistent weeding depth of 3–6 cm and stable spraying height. Combined with an adjustable spraying width and a "detection–feedback–adjustment" mechanism to prevent plant collisions, the vehicle is fully compatible with the agronomic requirements of narrow-row cultivation. Inspired by mole cricket forelegs, the vehicle's bionic weeding wheel blade model incorporates quantified biological features: quadratically fitted claw toe contours ($R^2 > 0.97$), a toe base height-to-width ratio of 1:2, and a toe groove radius-to-toe height ratio of 1:1. This design achieves a reliable biological-to-engineering translation. EDEM-based Discrete Element Method (DEM) simulations confirm that the bionic wheel outperforms conventional designs: the average torque is 17.4% lower (7.75 vs. 9.38 N·m), the soil disturbance rate is 8.2 percentage points higher (95.2% vs. 87.0%), and soil particle motion is more ordered (average velocity: 0.52 vs. 0.58 m/s), effectively reducing energy waste and improving weeding efficiency.

Keywords: sesame weeding; bionic blade; integrated work vehicle; discrete element simulation

Check for updates

Academic Editors: Gabriel Henrique Horta de Oliveira and Redmond R. Shamshiri

Received: 18 November 2025
Revised: 29 December 2025
Accepted: 6 January 2026
Published: 3 May 2026

Copyright: © 2026 by the authors. Licensee MDPI, Basel, Switzerland. This article is an open access article distributed under the terms and conditions of the Creative Commons Attribution (CC BY) license.

1. Introduction

The Huanghuaihai region is China's primary sesame-producing area and possesses climatic and soil conditions well suited for sesame cultivation [1]. Nevertheless, field management faces significant challenges, as the mechanization of key practices essential for yield and quality—including cultivation, weed control, and plant protection spraying—has encountered substantial bottlenecks [2]. The narrow row spacing of sesame, typically around 40 cm, limits the applicability of conventional machinery, which often causes root and plant damage during operation, whereas manual weeding incurs substantial labor costs. Weeds compete with crops for resources and promote the proliferation of pests and diseases, leading to yield losses of 30–40% in severely affected fields and a reduction in seed oil content [3]. In pest and disease management, pathogens such as stem tip blight and pests like aphids demand narrow, precise treatment windows. Current equipment is often plagued by uneven droplet distribution and inadequate coverage, which not only

hinders effective pest management during critical growth stages but also poses risks of environmental pollution and pesticide residues [4].

Since the beginning of the 21st century, agricultural mechanization has advanced steadily, with mechanical weeding emerging as a mainstream approach [5]. Compared with traditional chemical and manual weeding methods, mechanical weeding offers unique advantages: it effectively mitigates environmental pollution, enhances soil properties during tillage, and thus complies with conservation tillage principles [6]. After years of development, weeding machinery has become diversified, and weeding wheels have been widely adopted by farmers due to their stable performance, high weeding efficiency, and ability to prevent ridge formation during operation [7]. However, the weeding blades of these wheels encounter substantial resistance during soil penetration [8] and are prone to soil adhesion during soil exit, both of which severely impair weeding efficiency [9,10]. Current strategies to reduce soil penetration resistance include redesigning blade structures [11], improving blade materials [12], and optimizing blade installation angles [13]. In recent years, automated weeding and spraying technology has begun to develop rapidly toward precision, energy efficiency, and multi-functional integration [14–16]. The integration of bionic design with discrete element method (DEM) simulation has emerged as a promising approach for reducing weeding resistance and enhancing operational adaptability [17]. Nevertheless, a technical gap persists in specialized automated weeding equipment for sesame cultivation with narrow row spacing, as conventional automated machinery generally exhibits poor adaptability to narrow row spacing and excessive energy consumption, severely restricting its field application [18,19].

To address the poor mechanical adaptability to narrow-row (40 cm) sesame cultivation and the high weeding resistance and energy consumption of conventional tools, this study aims to develop a bionic integrated vehicle for weeding and plant protection, verify the advantages of bionic design in reducing energy consumption and improving weeding efficiency, and ultimately provide technical support for mechanized sesame production.

2. Overall Design of the Integrated Operation Vehicle

2.1. Design Criteria

Throughout the sesame growth cycle, two to three weeding operations are required. The first operation is conducted 10–15 days after seedling emergence, the second when plants reach a height of 20–30 cm, and the third prior to canopy closure. The weeding depth must be strictly controlled within the range of 3–6 cm. Insufficient depth results in ineffective weed removal and poor soil aeration, whereas excessive depth increases the risk of crop root damage [20].

Pesticide applications should be carried out during the early stages of disease development or when pests are in the early larval stage. This necessitates uniform droplet distribution and adequate canopy coverage while minimizing spray drift and pesticide residues to ensure control efficacy and environmental safety [21].

Accordingly, the design of the integrated operation vehicle must satisfy the following criteria: ① compatibility with a row spacing of 40 cm and agile maneuverability to minimize contact with plants; ② an adjustable weeding mechanism in both height and width to accommodate row spacing of 400 mm and a tillage depth of 3–6 cm; ③ a dynamically height-adjustable spraying mechanism to adapt to plant growth and improve the efficiency of pesticide use; ④ a compact and integrated structural design enabling simultaneous weeding and spraying across multiple rows per pass, thereby enhancing operational efficiency and reducing production costs.

2.2. Overall Structural Design of the Integrated Operation Vehicle

2.2.1. Overall Structure and Key Parameters

The vehicle's integral frame is fabricated by cutting and welding steel tubes and sheet metal components, ensuring sufficient structural strength for field operations. The powertrain adopts an extended-range hybrid configuration with a dual-energy supply system comprising a diesel generator and a battery pack. Specifically, four 12 V, 20 Ah batteries are connected in series to form a 48 V battery pack, which is continuously supplemented by a 5 kW diesel range-extending generator. When coupled with a 48 V, 3 kW high-torque servo motor and its corresponding control system, this configuration enables precise regulation of operating speed and key parameters, thereby providing stable and reliable power for efficient field operations. Interconnected functional modules form an integrated unit capable of performing three primary functions: vehicle mobility, mechanical weeding, and crop protection operations, as illustrated in Figure 1. The main components include a front-wheel steering mechanism, control panel, chemical tank, range-extending generator, control box, rear-wheel assembly, rear-axle motor, integral frame, seat, throttle and brake controls, battery pack, work platform, and operational unit.

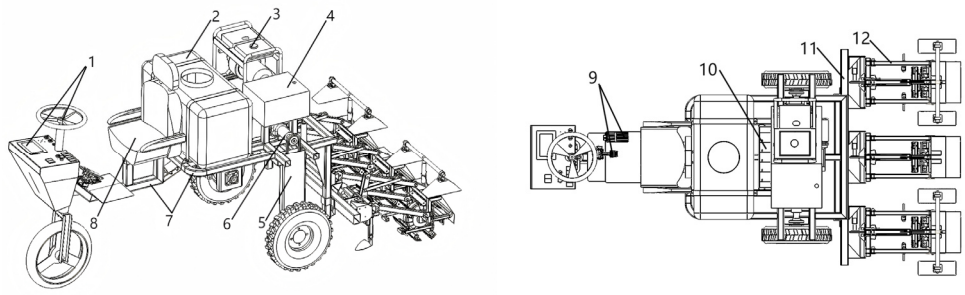


Figure 1. Overall structure of the operation vehicle. 1—Front wheel steering mechanism and control panel. 2—Fuel tank. 3—Range-extended generator. 4—Control box. 5—Rear wheel frame assembly. 6—Rear axle motor. 7—Integral frame. 8—Seat. 9—Accelerator and brake. 10—Battery pack. 11—Workbench. 12—Operational unit.

The key design parameters of the vehicle are presented in Table 1. The overall dimensions of the vehicle are 3000 mm × 1400 mm × 1600 mm, with a total mass of 680 kg, a chemical tank capacity of 200 L, and a maximum mounting capacity of three working units. The front and rear wheels have diameters of 560 mm and 510 mm, respectively, and the vehicle is driven by a single motor. These parameters are designed to meet the operational requirements of narrow-row sesame cultivation.

Table 1. Main structural parameters of the operational vehicle.

Parameter	Numeric Value
Size (length × width × height)/mm	3000 × 1400 × 1600
Total weight/kg	680
Battery count	4
Medicine cabinet capacity/L	200
Number of operational unit/units	3
Front wheel diameter/mm	560
Rear wheel diameter/mm	510
Number of drive motors/units	1

2.2.2. Working Principle

Guided by a modular design philosophy, the weeding mechanism and crop protection spraying mechanism are integrated into a single operational unit. Three such units

are synchronously mounted on the vehicle's rear work platform, enabling a combined operational mode of three-row parallel weeding and four-row simultaneous spraying; this configuration significantly improves operational efficiency, as illustrated in Figure 2.

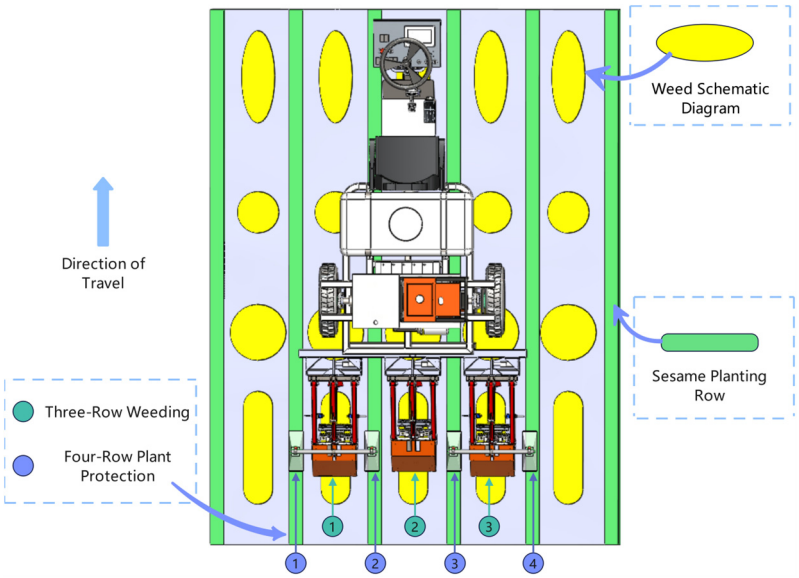


Figure 2. Schematic diagram of working principle.

During field operations, the electronic control system actuates the electric cylinders on the work platform to adjust the working height of each operational unit. As the vehicle advances, the weeding wheels installed beneath each unit rotate to uproot inter-row weeds, while the crop protection spraying system mounted on the upper part of the unit simultaneously applies pesticides. Each operational unit is equipped with a four-bar linkage limiting mechanism that automatically adapts to ground undulations, ensuring a consistent weeding depth and spraying height and thereby maintaining stable and continuous operation. Limit switches installed on both sides of each operational unit are fitted with probes that continuously monitor the lateral distance between the unit and the sesame plants. When an operational unit approaches a plant, the probe deflects and activates the corresponding circuit. The control system then drives the width adjustment mechanism to reverse the lateral movement of the unit, forming a closed-loop "detection–feedback–adjustment" control strategy that effectively prevents collisions with crop plants.

2.3. Design Structural Design of the Field Operation Vehicle

The main frame section is arranged horizontally, while the front and rear wheel frames provide vertical support to the upper frame, forming a rigid and integrated structure that ensures stability and reliability during operation. As illustrated in Figure 3, the vehicle frame consists of four main components: 1. the front-wheel steering section; 2. the middle load-bearing frame section; 3. the rear-wheel drive section; and 4. the rear workbench section.

The front-wheel steering section integrates key components, including the front wheels, control panel, steering wheel, and searchlights. The control panel is equipped with mechanical buttons for startup, forward and backward movement, and emergency stop, and it provides a real-time display of operational information while coordinating the management of all vehicle systems to ensure operational convenience and efficiency. As a critical structural component connecting the front-wheel steering and rear-wheel drive sections,

the middle load-bearing frame primarily supports core functional modules, including the chemical tank, generator, battery pack, and rear-axle motor.



(**a**) (**b**)

Figure 3. Schematic diagram of operational vehicle frame and physical image: (**a**) physical image; (**b**) Schematic diagram of operational vehicle frame.

Serving as the power core of the vehicle, the rear-wheel drive section comprises an extended-range generator, a battery pack, a rear-axle motor, and a chain transmission system. The hybrid power configuration effectively overcomes the range limitations of pure electric vehicles and reduces energy consumption and emissions by more than 30% compared with conventional fuel-driven systems. The rear-axle motor drives the rear wheels synchronously through chain transmission, thereby improving vehicle passability on complex terrain. The rear workbench section consists of components such as an electric cylinder, unit mounting brackets, and a work frame. It is used for installing the operational units, and its working height can be adjusted via electric cylinders to accommodate different operational scenarios. The rear-wheel drive section and the rear workbench section are illustrated in Figure 4.

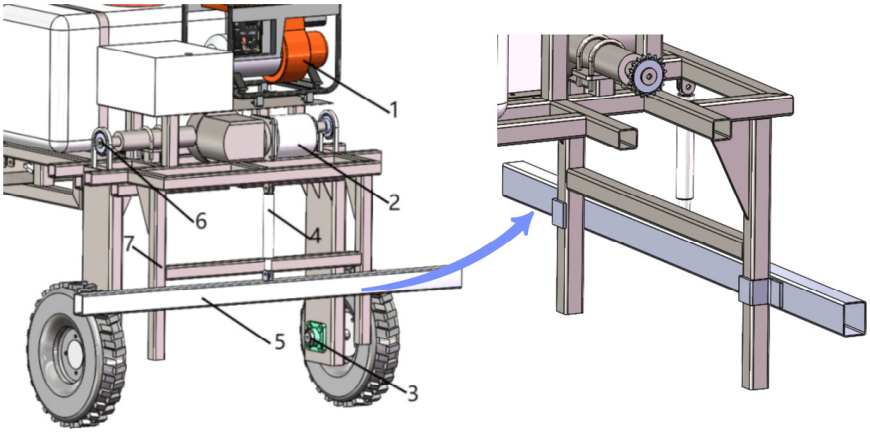


Figure 4. Schematic diagram of the rear-wheel section and workbench. 1—Range-extended generator. 2—Rear axle motor. 3—Square base bearing. 4—Electric cylinder. 5—Unit mounting bracket. 6—Chain drive system. 7—Working frame.

2.4. Design of the Integrated Weeding and Crop Protection Spraying Mechanism

2.4.1. Structure and Working Principle of the Integrated Weeding-Crop Protection Unit

The integrated weeding and crop protection spraying unit, the core innovative structure of this study, enables efficient coordinated inter-row cultivation, weed control, and

crop protection spraying for sesame field management via integration and modularization principles, as illustrated in Figure 5. It features a stacked architecture: the lower layer houses the mechanical weeding mechanism, and the upper layer mounts the plant protection system, with functional linkage achieved through a parallel linkage frame and dedicated control system.

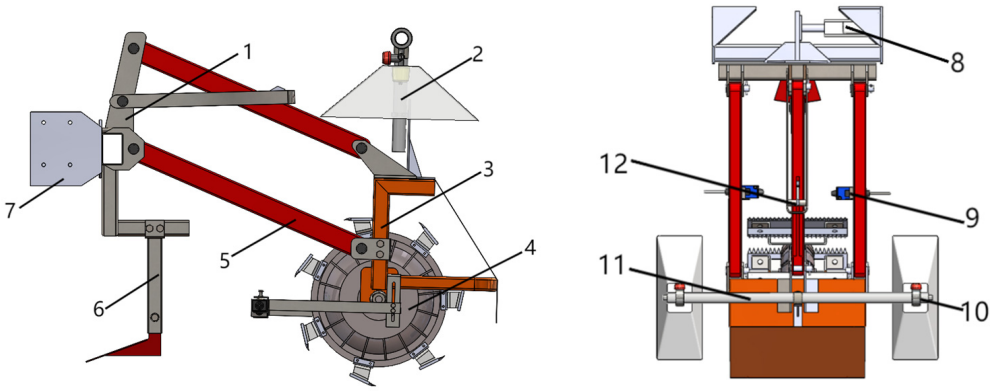


Figure 5. Schematic diagram of the operational unit's structure. 1—Mounting bracket. 2—Plant protection cover. 3—Weeding wheel frame. 4—Weeding wheel. 5—Parallel linkage mechanism. 6—Soil loosening blade. 7—Width adjustment bracket. 8—Electric cylinder. 9—Limit switch. 10—Nozzle. 11—Plant protection rack. 12—Sliding block limit mechanism.

The mechanical weeding mechanism includes a biomimetic weeding wheel with uniformly distributed blade teeth optimized from mole cricket foreleg claw and toe morphology; it is hub motor-driven for high-speed rotational cutting. It also includes a front-mounted soil-loosening blade that pre-loosens topsoil to facilitate wheel penetration. The plant protection system comprises a support frame, nozzles with adjustable spacing and height based on crop morphology, adjustment devices, and a protective cover.

During operation, the front-mounted blade loosens the surface soil, while the biomimetic weeding wheel cuts weeds along a residual cycloidal trajectory, together ensuring a weeding depth of 3–6 cm. The spraying system adjusts both height and width to achieve precise pesticide application. The parallel linkage and width adjustment mechanisms jointly constitute a terrain-adaptive system, ensuring stable operation under complex field conditions.

2.4.2. Design of the Bionic Mechanical Weeding Wheel

The first claw toe of the mole cricket foreleg has evolved into a distinctive wedge-shaped structure, which enables efficient soil penetration while increasing the soil contact area. Its high digging efficiency and strong environmental adaptability make it an ideal biomimetic prototype for the design of weeding blade teeth. To address the insufficient digging force and poor soil penetration of conventional blades under complex soil conditions, bionic blade teeth inspired by mole cricket claws adopt this wedge-shaped configuration, allowing smooth soil penetration and effective severing of weed roots.

The biomimetic blade teeth are uniformly distributed on the weeding wheel in a pattern analogous to the arrangement of mole cricket foreleg claws, as illustrated in Figure 6. The blade teeth are tightly integrated with the blade holder, thereby maintaining structural stability under high-speed rotation and complex mechanical loads. Arranged circumferentially around the hub motor, the blade teeth utilize the motor's output to achieve efficient rotational motion that mimics the rapid digging behavior of mole crickets, while their circular configuration ensures sequential and orderly contact with the soil.

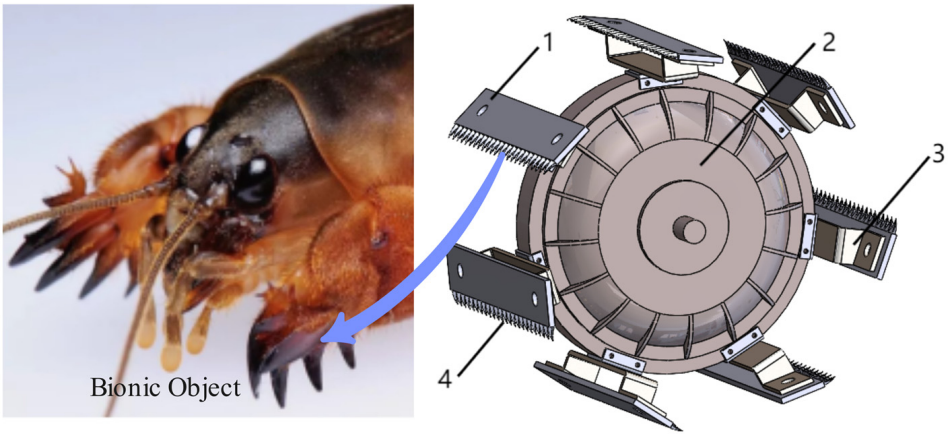


Figure 6. Schematic diagram of the biomimetic weeding wheel. 1—Weeding blade. 2—Hub motor. 3—Blade holder. 4—Bionic blade teeth.

2.4.3. Motion Analysis of the Weeding Wheel and Design of the Blade Group

The motion of the weeding wheel consists of two components: uniform linear translation in the horizontal direction and uniform circular motion about its rotational axis. This combined motion enables continuous and uniform weeding operations. During operation, the circumferentially arranged weeding blades cut sequentially, and the cutting path of each blade follows a cycloidal trajectory, as illustrated in Figure 7.

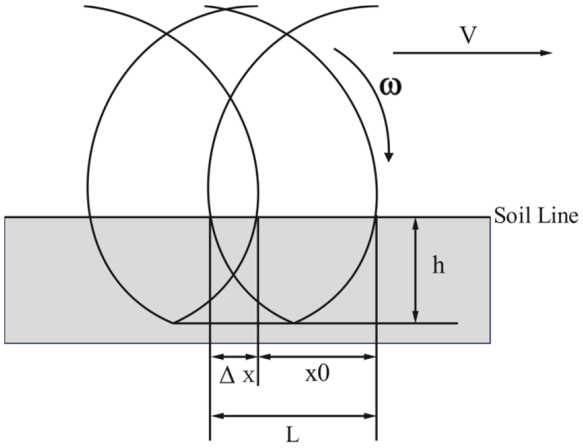


Figure 7. Schematic diagram of the blade's movement trajectory.

The motion trajectories of two adjacent blades are identical, differing only by a translational displacement of x_0. The overlapping distance between their trajectory curves along the soil surface is given by:

$$\Delta x = L - x_0 \quad (1)$$

In Equation (1), L denotes the length of the arc formed by the intersection between the residual trajectory of the weeding blade and the soil surface, and x_0 represents the distance between two adjacent intersection points of the residual trajectories with the soil surface. The penetration depth of the weeding blade is denoted by h. The overlap distance Δx directly affects the effectiveness of the weeding operation. To prevent missed weeding, it must be ensured that $\Delta x > 0$.

A coordinate system is established with the lowest point of the epicycloid selected as the origin, as illustrated in Figure 8, and the motion trajectory equation of a single weeding blade is derived. The initial state is defined as the moment when the blade is located at the lowest point (point A1 in the diagram). Let O1 denote the instantaneous center of the

weeding wheel, and let the line connecting O1 and A1 represent the working radius of the wheel, denoted by R. When the weeding wheel rotates with an angular velocity ω and simultaneously translates forward at a velocity v for a duration of t, point A1 rotates to position A2, while the center point O1 shifts to position O2. Let ϕ denote the rotation angle, let d_0 denote the translational displacement of the wheel center, and let (x, y) represent the coordinates of point A2. The motion trajectory of the blade tip can then be expressed as follows:

$$\begin{cases} x = d_0 - R\sin\theta \\ y = R - R\cos\theta \end{cases} \tag{2}$$

Based on the above conditions, the following relations can be obtained:

$$d_0 = vt = \frac{\theta}{\omega}v \tag{3}$$

Substituting d_0 into Equation (2) and simplifying yields

$$\begin{cases} x = \frac{v\phi}{\omega} - R\sin\theta \\ y = R(1 - \cos\theta) \end{cases} \tag{4}$$

Equation (4) yields $\cos\theta = 1 - \frac{\gamma}{R}$, $\theta = \arccos(1 - \frac{\gamma}{R})$, $\cos^2\theta + \sin^2\theta = 1$. It follows that

$$\sin\theta = \sqrt{\frac{y}{R}\left(2 - \frac{y}{R}\right)} \tag{5}$$

By substituting the original expressions to eliminate the parameters, the following relation is obtained:

$$x = \left|\frac{v}{\omega}\arccos(1 - \frac{y}{R}) - \sqrt{y(2R - y)}\right| \tag{6}$$

$$L = 2|x| = 2\left|\frac{v}{\omega}\arccos(1 - \frac{y}{R}) - \sqrt{y(2R - y)}\right| \tag{7}$$

Suppose Z cutting units are evenly spaced around the weed-cutting wheel. The time interval between two adjacent cutting units successively entering the soil for weed removal is $t = \frac{2\pi}{Z\omega}$. Then x_0 can be expressed as

$$x_0 = d_0 = vt = \frac{2\pi}{Z\omega}v \tag{8}$$

By substituting the above expression into Equation (1), the following relation is obtained:

$$\Delta x = L - x_0 = 2\left|\frac{v}{\omega}\arccos\left(1 - \frac{y}{R}\right) - \sqrt{y(2R - y)}\right| - \frac{2\pi}{Z\omega}v \tag{9}$$

To make Δx greater than 0, the number of cutting units Z must satisfy

$$Z > \frac{\pi v}{\omega\left|\frac{v}{\omega}arccos\left(1 - \frac{h}{R}\right) - \sqrt{h(2R - h)}\right|} \tag{10}$$

Given the weeding radius R = 170 mm, weeding depth h ranging from 30–60 mm, angular velocity ω between 5π–7π/s, and forward speed v in 0.3–1.3 m/s, substituting these parameters into the formula yields $Z > 4.55$. After rounding to the nearest integer, $Z \geq 5$ is obtained. To ensure optimal weeding efficiency and operational reliability, a seven-blade group weeding wheel configuration is ultimately adopted in this study, with seven blade groups uniformly distributed along the circumference of the hub motor.

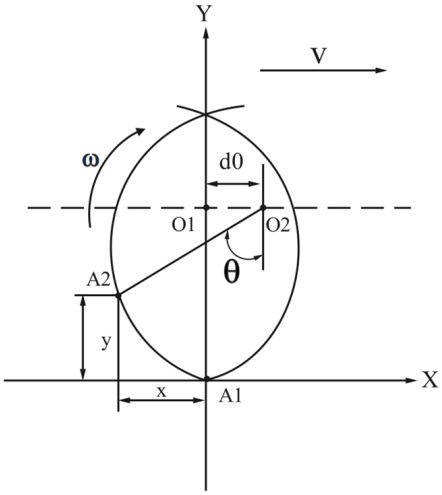


Figure 8. Schematic diagram of the trajectory coordinate system.

2.4.4. Design of the Single Operational Unit Frame

As illustrated in Figure 9, the frame structure of a single operational unit is divided into four main components: 1. the width adjustment frame, which is used to mount the unit onto the operation vehicle and to adjust the working width of the weeding wheels and the crop protection spraying mechanism; 2. the load-bearing frame, which connects the sliding table of the width adjustment mechanism to the parallel linkage system; 3. the parallel linkages, which provide terrain adaptability; and 4. the wheel carrier frame, which supports the weeding wheels and accommodates the limit switch and the crop protection spraying mechanism.

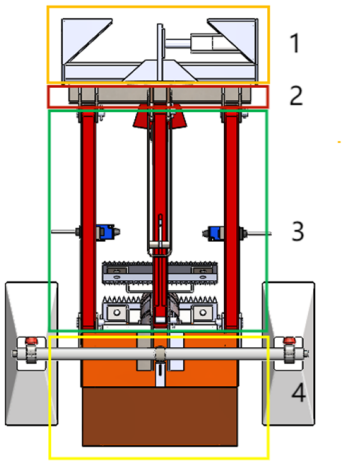


Figure 9. Schematic diagram of the operational unit frame.

The width adjustment frame comprises a fixed frame, an electric cylinder, slide rails, and a sliding table, as shown in Figure 10. The sliding table is rigidly connected to the rear load-bearing frame via U-bolts, and the electric cylinder pushes the sliding table along the slide rails—this movement adjusts the working width of the weeding wheels and plant protection mechanism.

To adapt to complex field terrains, the integrated parallel linkage damping mechanism combines a parallel linkage system with a slider-based damping mechanism, as illustrated in Figure 11. Owing to its specially designed degrees of freedom, the mechanism enables vertical terrain adaptation while simultaneously providing shock absorption and height limitation.

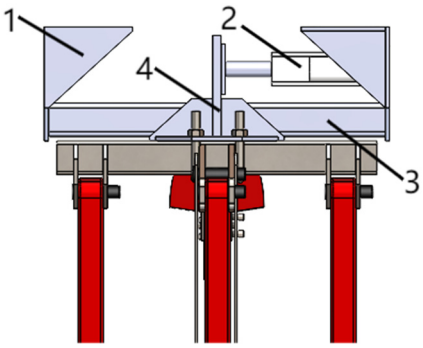


Figure 10. Schematic diagram of the width-adjusting structure. 1—Fixed frame. 2—Electric cylinder. 3—Slide rail. 4—Slide table.

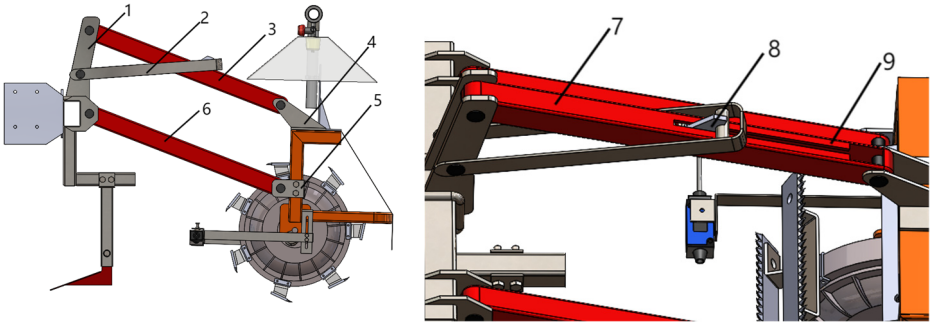


Figure 11. Schematic diagram of the parallel linkage structure. 1—Carrier bracket. 2—Limiting bracket. 3—Upper connecting rod. 4—Upper fixed bracket for connecting rod. 5—Lower support bracket for connecting rod. 6—Lower connecting rod. 7—Internal spring. 8—Limiting and delaying slider. 9—Slide table.

This mechanism incorporates a specially designed degree-of-freedom configuration, enabling vertical self-adaptation of individual operational units while providing effective shock absorption and height control. When the vehicle operates on uneven terrain, the parallel linkage mechanism automatically adjusts the height of each unit to maintain the preset working positions of the functional components. A buffering system composed of limiting sliders and guide frames absorbs impact energy generated during the movement of the weeding wheel carrier. As illustrated in Figure 12, when the sliders move along the guide rails, the internal springs dissipate energy induced by sudden terrain variations and simultaneously apply downward pressure to the weeding wheels. The length of the guide rails constrains the maximum lifting height of the wheel carrier, thereby ensuring sufficient weeding depth and preventing failures in pesticide application.

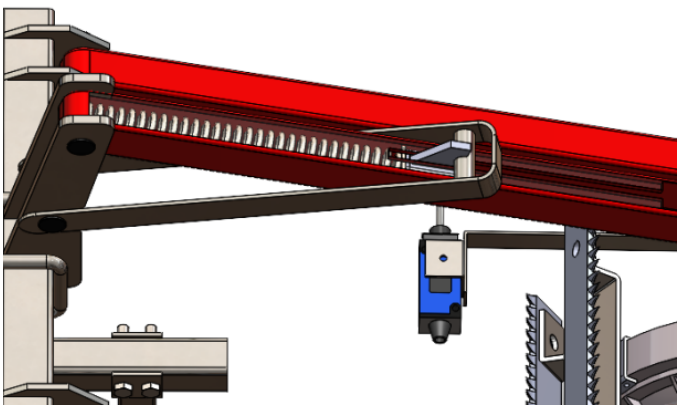


Figure 12. Schematic diagram of the linkage interior.

The wheel platform assembly is shown in Figure 13a. The hub motor bracket securely fastens the weeding wheel to ensure operational stability, while the rear side panel minimizes debris and soil splatter to protect sesame plants. Limit switches are mounted on both sides of the wheel platform via height adjustment brackets and extension brackets; when combined with U-shaped clamps, these components enable flexible adjustment of working height and width to adapt to sesame growth stages.

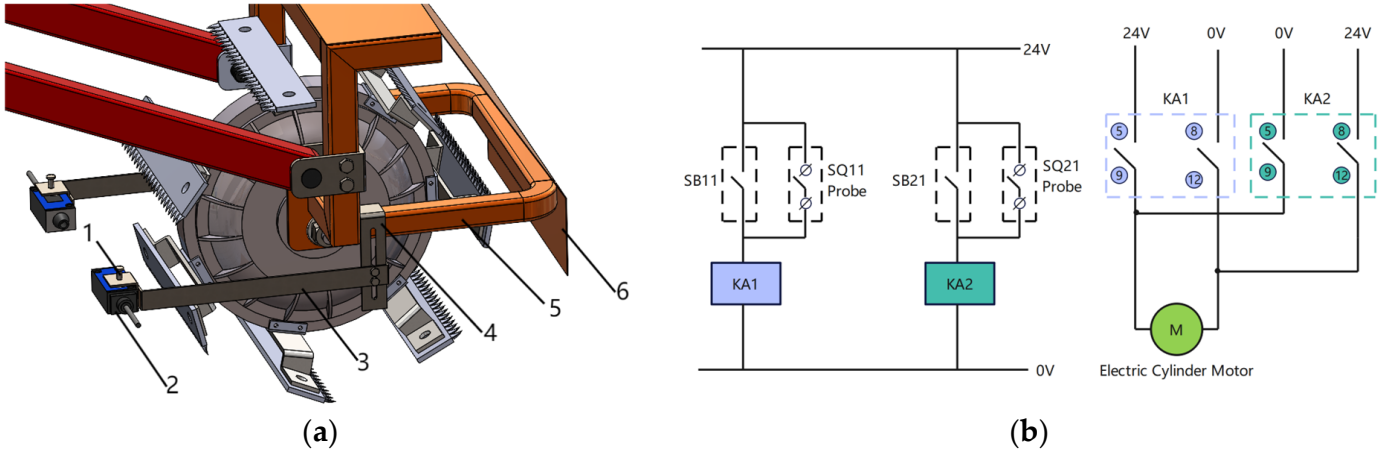


Figure 13. Wheel platform structure and control circuit diagram: (**a**) structural diagram of the wheel platform; (**b**) width adjustment circuit diagram. 1—U-shaped clamp. 2—Limit switch. 3—Extension bracket. 4—Height adjustment bracket. 5—Hub motor mounting bracket. 6—Stop plate.

As illustrated in Figure 13b, during the equipment operation, the probes of the limit switches (SQ11 and SQ21) continuously monitor the lateral distance between the wheel platform and sesame plants. When either probe comes into contact with the sesame seedlings on both sides, the corresponding circuit is activated and sends a signal to the control system, which then triggers relay KA1 or KA2: the normally open contacts (5 and 9, 8 and 12) of the relay close, and the power supply polarity is adjusted simultaneously to drive the electric cylinder to rotate forward or reverse, thereby driving the overall lateral translation of the operational wheel platform until the probe is disconnected from the sesame seedlings. It is important to note that if both probes are triggered simultaneously, the circuit will trigger a short-circuit protection mechanism, which stops the electric cylinder motor immediately. This design forms a "detection–feedback–adjustment" closed-loop system with a safety interlock function, which can effectively prevent the operational unit from colliding with plants and ensure operational accuracy.

2.4.5. Design of the Crop Protection Structure

The crop protection nozzle is integrated into the frame of the wheel platform assembly via a crop protection rack, forming a precision pesticide application system, as illustrated in Figure 14. Structurally, the nozzle adopts a 20 mm snap-fit connection, allowing rapid assembly and disassembly with the pipe rack. The T-shaped pipe rack consists of two PVC pipes with a diameter of 20 mm connected by pipe clamps. The horizontal main pipe supports the crop protection nozzle, while the vertical support pipe is connected to the midpoint of the horizontal pipe to provide structural stability.

The pipe rack enables bidirectional adjustment. A slot on the crop protection nozzle engages with the horizontal main pipe, allowing lateral sliding to adjust the working width and accommodate different row spacings. The vertical support pipe is equipped with quick-release clamps, enabling vertical height adjustment by sliding the T-shaped pipe rack, thereby adapting to variations in plant height at different sesame growth stages. For

precise pesticide application, the nozzle is fitted with a customized injection-molded crop protection cover, which reduces wind interference, restricts the spray range, concentrates pesticide deposition on sesame crowns, improves pesticide utilization efficiency, and reduces the risk of environmental pollution.

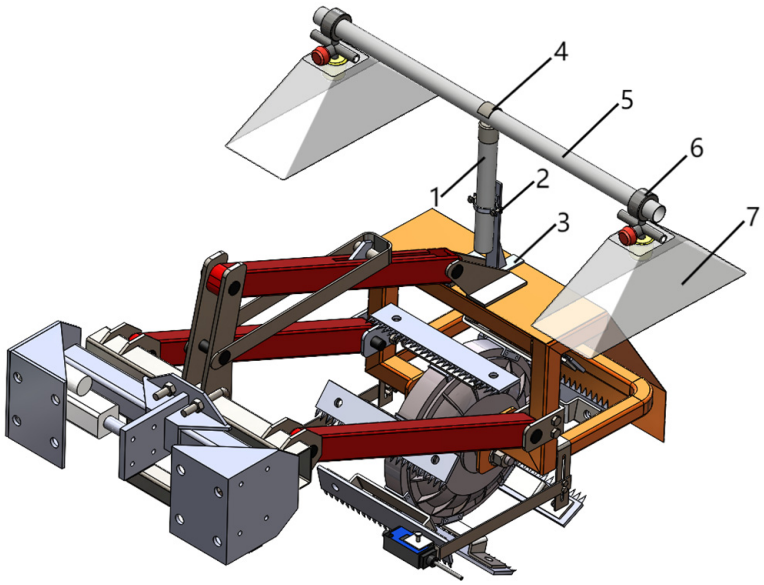


Figure 14. Schematic diagram of the crop protection structure. 1—Vertical branch pipe. 2—Clamp. 3—Plant protection mechanism mounting bracket. 4—Pipe clamp. 5—Horizontal main pipe. 6—Nozzle. 7—Cover.

3. Construction of the Bionic Blade Tooth Model

3.1. Biological Characteristics of Mole Cricket Forelegs

The mole cricket is a typical soil-dwelling insect commonly found in farmland and sandy loam soils. It inhabits underground environments at depths of approximately 10–20 cm, where it excavates tunnels for survival. Through long-term adaptation to soil conditions, the mole cricket has evolved distinctive anatomical features. Its forelegs, equipped with specialized claws that are thick and outward-curving, constitute the primary digging apparatus, while the curved geometry of the foreclaw digging structure effectively reduces soil resistance during burrowing, as illustrated in Figure 15.



Figure 15. Magnified view of the mole cricket's foreclaw.

The forelegs of the mole cricket are symmetrically distributed on both sides of the head, with the claw toe tips curved forward and outward. During the digging process, the claw

toes initially penetrate the soil and subsequently expand outward to enlarge the burrow. The forelegs comprise conventional anatomical components such as the tibia and tarsus. The inner and outer curved surfaces of the claw toes exhibit different curvature radii, with the upper portion forming a squared wedge-shaped profile and an included angle between the two sides of approximately 30–40° [22]. Previous studies have demonstrated that this wedge-shaped configuration effectively reduces soil pressure and contact resistance. Each foreleg of the mole cricket contains four closely arranged claw toes that collectively exhibit a wedge-shaped geometry, characterized by a thick base and a gradually tapering tip. This geometric arrangement provides a mechanical advantage for soil penetration and constitutes a key functional element of the mole cricket's digging mechanism.

3.2. Feature Curve Extraction of Mole Cricket Foreleg Claw Toes

3.2.1. Acquisition of Contour and Feature Point Coordinates

The first claw toe of the mole cricket was removed, and its lateral morphological features were imaged using a macro camera; the image was then imported into SolidWorks 2023 software as a sketch. A reference plane was selected to enter the sketch editing mode, where the image was aligned precisely with the coordinate axes. Meanwhile, the image width was uniformly set to 100 mm (with aspect ratio maintained) to facilitate subsequent fitting data extraction. The "Start Tracing Image" function was activated, and parameters such as image transparency and contrast were optimized to complete contour extraction and refinement [23]. After obtaining the contour line, 28 evenly distributed reference points were inserted and converted into entity references to accurately acquire the position coordinates of each point, as shown in Figure 16.

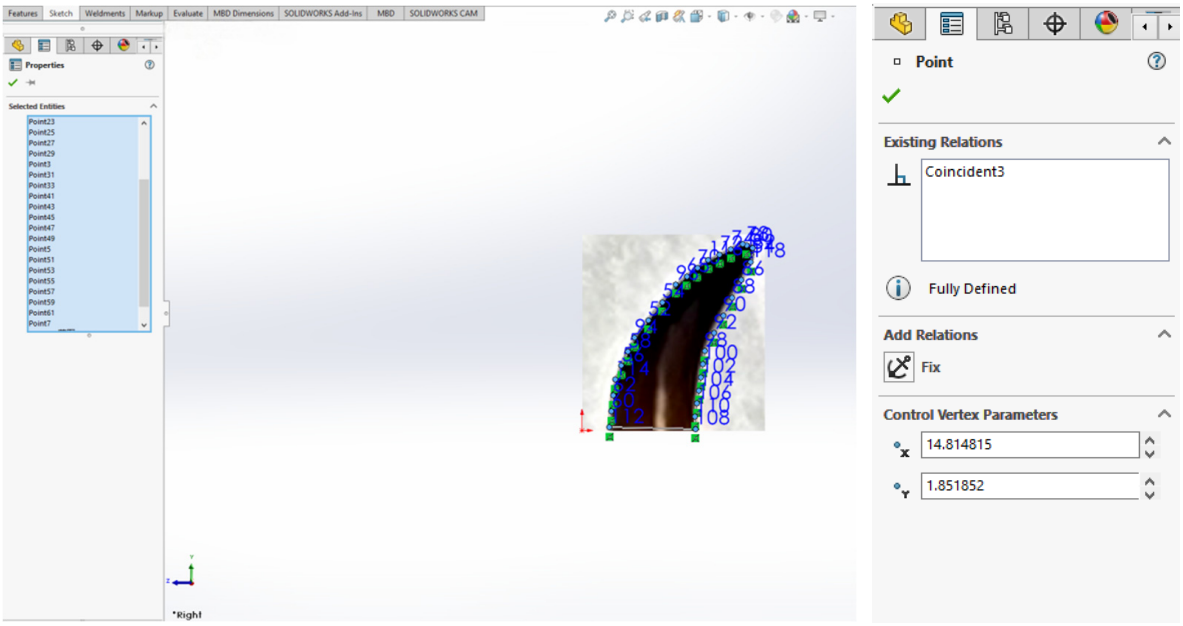


Figure 16. Diagram of feature point coordinate acquisition.

3.2.2. Fitting Analysis of the Outer Contour Curve

Based on the functional characteristics and contour curvature of the claw toe, the irregular tip region was excluded, and the remaining profile was divided into an outer contour and an inner contour. The outer contour consists of 16 feature points, with the corresponding coordinate data listed in Table 2. The X-coordinates range from 14.81 to 91.63, while the Y-coordinates exhibit an overall increasing trend, reaching a maximum

value of 101.6 at Point 15. This trend reflects the gradual morphological expansion of the outer contour from the base to the tip of the claw toe.

The analysis reveals that the outer contour curve adheres to the law of a quadratic function ($y = ax^2 + bx + c$). The fitted parameters are a = −0.0182, b = 3.038, and c = −26.965, with a coefficient of determination $R^2 = 0.97721$. The deviation between the fitted curve and the measured points is within 0.5 mm, which verifies the quadratic function characteristic of the outer contour and provides a reliable mathematical model for contact mechanics analysis. The fitting curve is shown in Figure 17.

Table 2. Outer contour feature point coordinates.

Order Number	X	Y
1	14.81	1.85
2	15.84	10.56
3	16.87	19.27
4	17.9	27.98
5	21.46	35.59
6	25.03	43.20
7	28.6	50.82
8	36.14	60.56
9	43.68	70.3
10	57.13	84.56
11	63.03	89.09
12	68.93	93.62
13	75.17	96.5
14	81.41	99.38
15	89.84	101.6
16	91.63	100.8

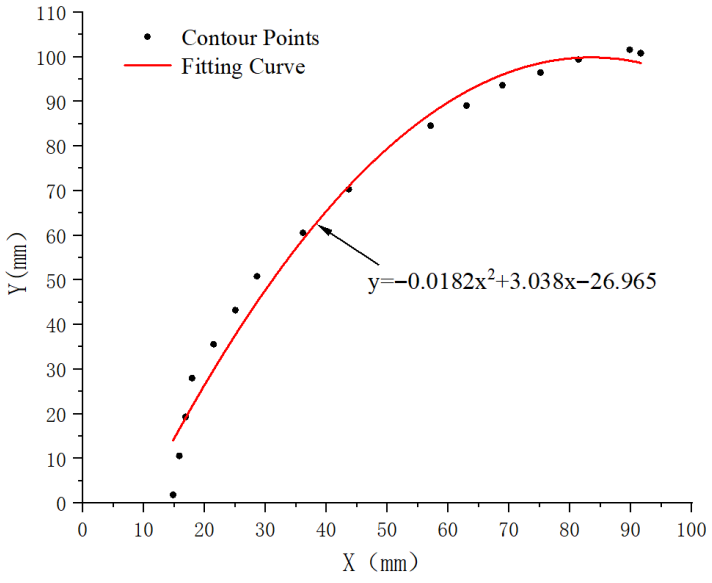


Figure 17. Diagram of the outer contour fitting curve.

3.2.3. Fitting Analysis of the Inner Contour Curve

For the inner contour, 12 feature points were extracted, with a spacing between adjacent points ranging from 0.7 to 1.1 mm. The corresponding coordinate data are provided in Table 3. The X-values range from 61.93 to 92.18, while the Y-values increase from 0.82 to 92.38, showing an overall upward-slanting extension. The direction of curvature is

consistent with that of the outer contour. Similarly, a quadratic function was used to fit the inner contour.

Table 3. Inner contour feature point coordinates.

Order Number	X	Y
1	61.93	0.82
2	61.73	7.61
3	62.8	14.81
4	63.87	22.02
5	64.94	29.22
6	66.01	36.42
7	68.89	43.62
8	72.1	53.37
9	76.12	63.13
10	81.14	72.88
11	87.16	84.633
12	92.18	92.38

The fitting parameters are a = −0.0794, b = 14.854, and c = −604.899, with a goodness-of-fit R^2 = 0.97454. This indicates a high degree of agreement between the fitted curve and the measured points, which meets the requirements of subsequent research. The fitting curve is shown in Figure 18.

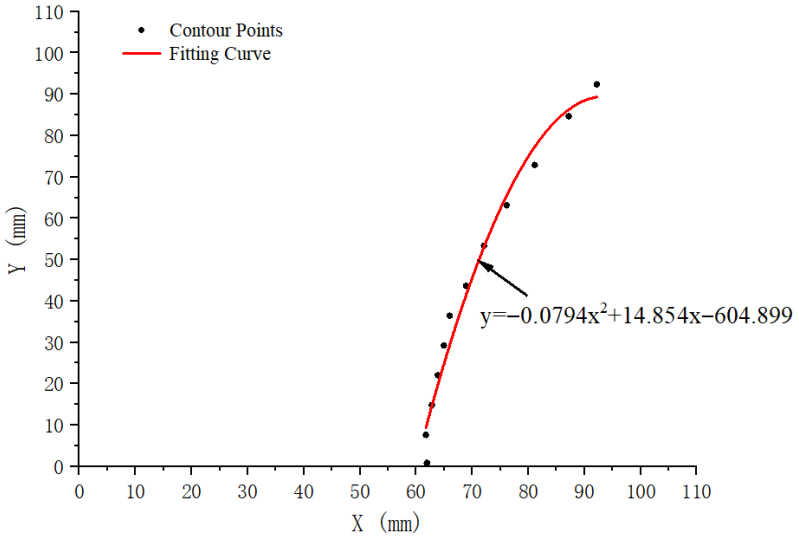


Figure 18. Diagram of the inner contour fitting curve.

3.2.4. Comprehensive Verification of Contour Curves

The curves of the outer and inner contours were merged into a unified coordinate system, as illustrated in Figure 19, achieving a smooth transition at the base of the claw toes (X = 14.81–61.93) with high morphological consistency to the original contours. Comparative analysis reveals that the absolute value of the second-order coefficient for the outer contour (0.0182) is lower than that of the inner contour (0.0794), indicating a gentler curvature that better satisfies stability requirements for primary contact surfaces. The differences in the first-order and constant terms reflect spatial positional deviations, demonstrating the asymmetrical morphology between the inner and outer surfaces of the claw toes.

In conclusion, both the internal and external contours follow the quadratic function model (R^2 > 0.97), which validates the quantification of claw and toe morphology and provides a foundation for 3D modeling and subsequent analysis.

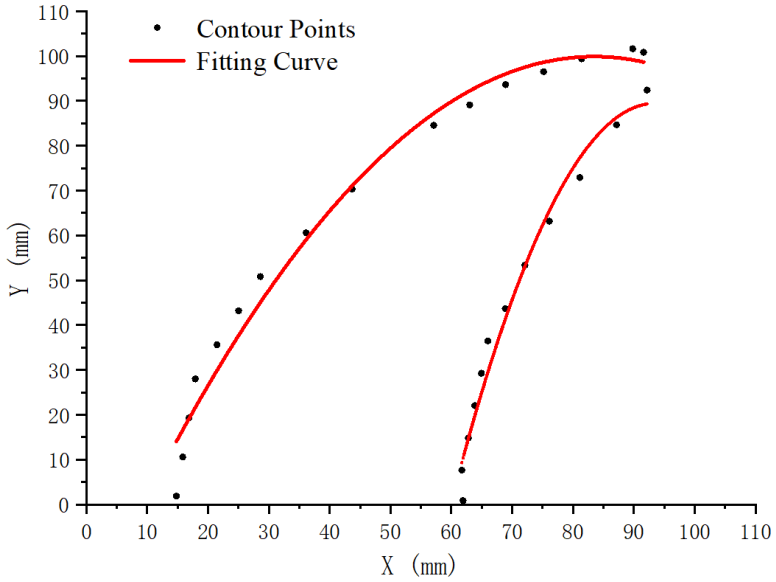


Figure 19. Diagram of the overall contour fitting curve.

3.3. Morphological Characteristic Analysis of Mole Cricket Claw Toe Base

The claw toe features a typical wedge shape—thick at the base and tapering toward the tip—to facilitate efficient soil penetration. Its base is roughly triangular, with concave arcs on both sides forming a unique toe groove structure. This design optimizes the smoothness of soil penetration, reduces frictional resistance, and increases the soil contact area, thereby enhancing gripping capacity and digging performance [24]. Quantitative measurements of the claw toe's basal cross-section, conducted using SolidWorks as shown in Figure 20, revealed a base height of 38.82 mm (measured between the highest and lowest points) and a width of 78.56 mm (measured between the leftmost and rightmost points), yielding an approximate height-to-width ratio of 1:2.02, close to 1:2.

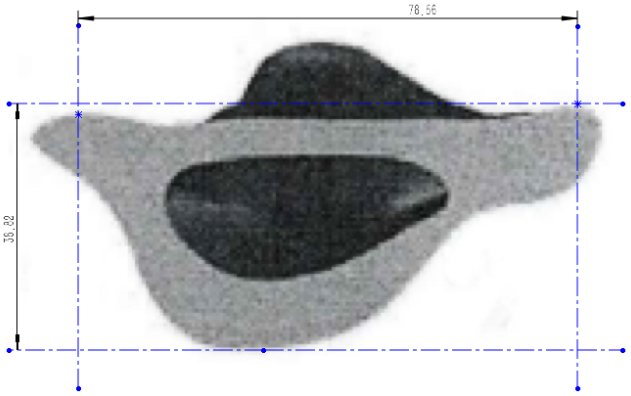


Figure 20. Diagram of toe base width and height measurement.

To quantify the arc radius of the toe groove, the contour of the toe groove region was extracted and optimized by adjusting image parameters, as shown in Figure 21. Since the left half of the mole cricket's left claw toe contacts the soil first during digging and has a more robust structure, it was selected as the research subject. Five evenly distributed reference points were marked on the left contour line, and their coordinates were recorded (see Table 4).

To fit the arc formed by the coordinate points (20.769, 24.16), (19.326, 29.131), (17.402, 33.46), (14.676, 37.308), and (11.472, 39.945) more accurately, the least squares method was used for circle equation fitting.

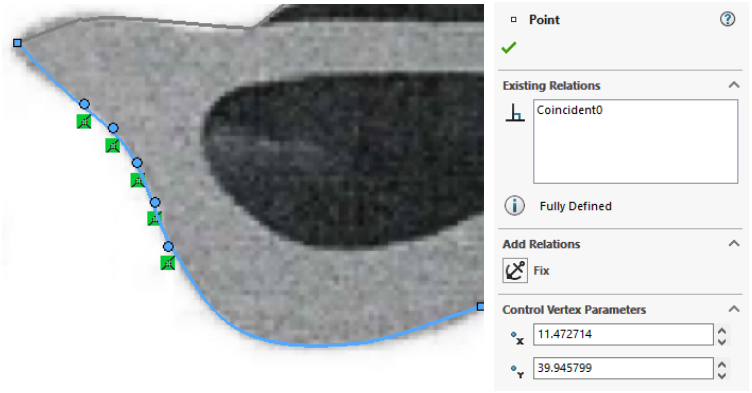


Figure 21. Schematic diagram of feature point acquisition in the toe groove region.

Table 4. Feature point coordinates of the toe groove region.

Order Number	X	Y
1	20.769	24.16
2	19.326	29.131
3	17.402	33.46
4	14.676	37.308
5	11.472	39.945

The core principle of the least squares method is to find a function curve (in this case, a circle) that minimizes the sum of squared deviations from a given set of data points. In the case of circle fitting using the equation $x^2 + y^2 + Dx + Ey + F = 0$, this is accomplished by adjusting the parameters D, E, and F to minimize the sum of squared errors when five points are substituted into the equation, thereby determining the circle that best fits the data points. Substituting the five points into the equation results in the following system of equations:

For point (20.769, 24.16): $20.769D + 24.16E + F = -1014.057$.
For point (19.326, 29.131): $19.326D + 29.131E + F = -1222.119$.
For point (17.402, 33.46): $17.402D + 33.46E + F = -1422.401$.
For point (14.676, 37.308): $14.676D + 37.308E + F = -1607.372$.
For point (11.472, 39.945): $11.472D + 39.945E + F = -1727.21$.
The above system of equations can be expressed in matrix form as $\boldsymbol{Ax = B}$, where

$$A = \begin{bmatrix} 20.769 & 24.16 & 1 \\ 19.326 & 29.131 & 1 \\ 17.402 & 33.46 & 1 \\ 14.676 & 37.308 & 1 \\ 11.472 & 39.945 & 1 \end{bmatrix}, x = \begin{bmatrix} D \\ E \\ F \end{bmatrix}, b = \begin{bmatrix} -1014.057 \\ -1222.119 \\ -1422.401 \\ -1607.372 \\ -1727.21 \end{bmatrix} \quad (11)$$

According to the least squares method, the normal equation is given by:

$$\left(A^T A\right) x = A^T b \quad (12)$$

After performing the calculations, the following results are obtained:

$$A^T A = \begin{bmatrix} 1322.57 & 1843.26 & 83.645 \\ 1843.26 & 2634.36 & 164.004 \\ 83.645 & 164.004 & 5 \end{bmatrix}, A^T b = \begin{bmatrix} -128806.6 \\ -182220.8 \\ -7093.16 \end{bmatrix} \quad (13)$$

Solving the normal equation yields the following parameters:

$$x = (A^T A)^{-1} A^T b \approx \begin{bmatrix} -112.28 \\ -45.76 \\ 1810.5 \end{bmatrix} \tag{14}$$

Therefore, the circle equation parameters are: $D = -112.28$, $E = -45.76$, $F = 1810.5$.

The standard form of a circle equation is $(x-a)^2 + (y-b)^2 = R^2$, where (a, b) is the center coordinate and R is the radius. The relationship between the standard form and the general form is: $a = -\frac{D}{2}$, $b = -\frac{E}{2}$, $R = \sqrt{a^2 + b^2 - F}$.

Substituting the parameters gives: $a \approx 56.14, b \approx 22.88, R \approx 43.18$.

By substituting the center coordinates (56.14, 22.88) and radius R into the circle equation, the distance from each of the five feature points to the center is calculated. These distances are compared with the radius, with details provided in Table 5.

Table 5. Distance from feature points to the center.

Point Coordinates	Distance (mm)	Bias (mm)
(20.769, 24.16)	35.40	7.78
(19.326, 29.131)	37.34	5.84
(17.402, 33.46)	40.16	3.02
(14.676, 37.308)	43.90	0.72
(11.472, 39.945)	47.82	4.64

Average deviation:

$$\frac{7.78 + 5.84 + 3.02 + 0.72 + 4.645}{5} \approx 4.4 \tag{15}$$

Residual Sum of Squares (RSS):

$$RSS = \sum_{i=1}^{5} (d_i - R)^2 \approx 125.81 \tag{16}$$

The average error is 4.4 mm and $RSS \approx 125.81$, which is relatively small compared to the overall deviation, indicating a good fitting effect. From the known conditions, the center of the fitted circle is determined as (56.14, 22.88), with a toe groove arc radius of 43.18 mm. This radius is close to the cross-sectional toe height of 39.03 mm, resulting in an approximate 1:1 ratio between the toe groove arc radius and toe height. Through measurement, the chord length of the toe groove arc accounts for approximately two-thirds of the total length of the toe base hypotenuse.

The 1:1 ratio between the arc radius and toe height, along with the 1:2 ratio of toe base height to toe base width, forms key quantitative indicators of the claw toe's morphological characteristics, establishing its unique morphological foundation. Using these features and parameters, a symmetric bionic diagram of the claw toe base was constructed in SolidWorks, as shown in Figure 22. In this diagram, the center of the toe groove arc lies on the perpendicular bisector of the hypotenuse, satisfying the following relationships: arc radius R: base height H = 1:1, and base toe width L:H = 1:2, and the chord length is approximately two-thirds of the total length of the toe base hypotenuse. This morphological diagram visually presents the structural characteristics, providing reliable data for analyzing structure-function correlations and forming a foundation for exploring excavation mechanisms and related bionic designs.

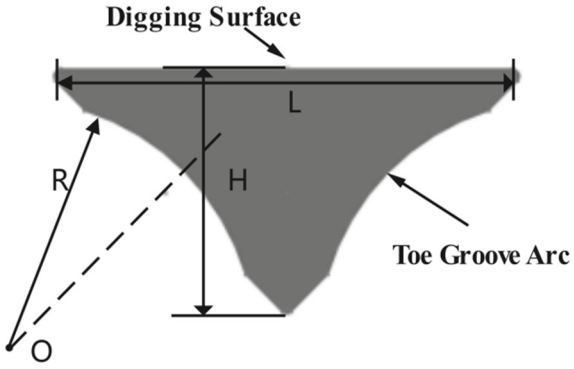


Figure 22. Symmetrical bionic diagram of the claw toe base.

3.4. Construction of the 3D Model for the Bionic Weeding Tool

3.4.1. Sketch Design of the XZ Plane (Upper Reference Plane)

The sketch on the XZ-plane represents the cross-section at the base of the claw toe. Based on the weeding operation requirements and blade standardization criteria, the toe base height (H) was set to 5 mm, matching the practical thickness of the weeding blade. Combined with the quantitative morphological analysis of the mole cricket's claw, the following geometric parameter rules were established: the ratio of toe height (H) to toe groove arc radius (R) is 1:1, the chord length is approximately two-thirds of the total length of the toe base hypotenuse, and the ratio of H to toe width (L) is 1:2. From these rules, L = 10 mm and R = 5 mm were derived, with the base cross-section designed as an axisymmetric figure. A sketch was then constructed on the reference plane in SolidWorks, with rounded corners to optimize structural continuity, as shown in Figure 23.

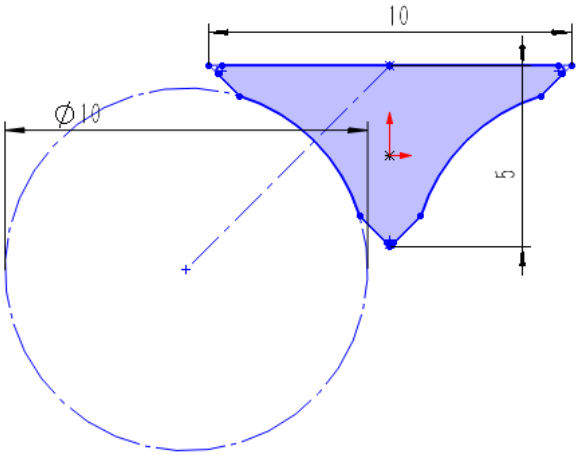


Figure 23. Sketch of the claw toe base.

3.4.2. Sketch Design of the XY Plane (Right Datum Plane)

A sketch was created on the Right View Reference Plane in SolidWorks, where the "Equation-Driven Curve" function was used to input the outer contour curve equation ($y = -0.0182x^2 + 3.038x - 26.965$, value range: 14.81–81.41) and inner contour curve equation ($y = -0.079x^2 + 14.854x - 604.899$, value range: 61.93–81.14). To align with the standardized tool base design, the lower endpoints of the two curves were connected with a horizontal line (initial spacing: 48 mm), and the overall contour was scaled by a ratio of 0.1041 (5/48) to reduce the endpoint spacing to 5 mm—achieving collaborative constraints between biological morphology and engineering dimensions. The claw toe tip was finalized with an arc: the inner-outer included angle was constrained to 35°, and the arc

was smoothly connected to the contour curves to replicate biological cutting characteristics, as shown in Figure 24.

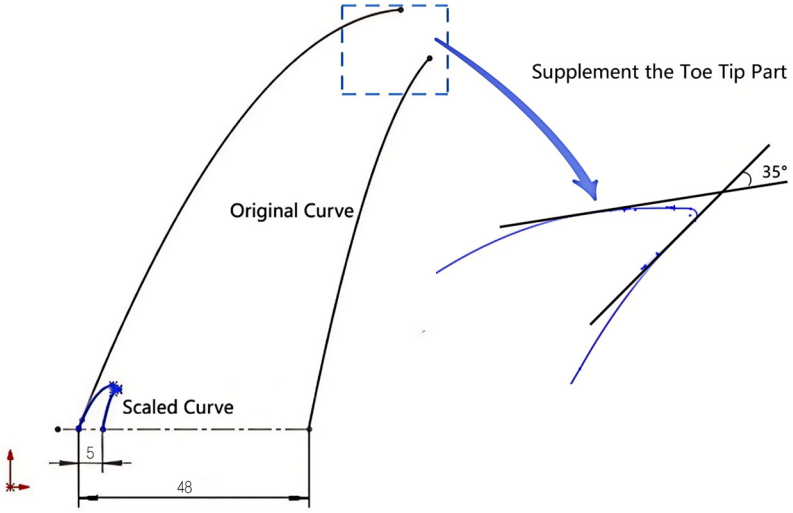


Figure 24. Diagram of toe contour construction.

3.4.3. Establishment of the Bionic Tool 3D Model

The single claw toe was modeled in SolidWorks using the Loft command. A reference plane was first created 5 mm away from the XZ-plane, and the scaled sketch from the XZ-plane was employed as the middle cross-section, sandwiched between the sketches on the XY-plane. The XZ-plane sketch served as the bottom contour, the middle cross-section as the middle constraint, and the tip vertex as the top convergence constraint. The curves from the XY-plane sketch were then used as guide curves to generate the claw toe's longitudinal morphology. This modeling approach ensured high fidelity to the biological characteristics of the mole cricket's claw toe. A comparison between the single claw toe model and 3D scanning data is presented in Figure 25.

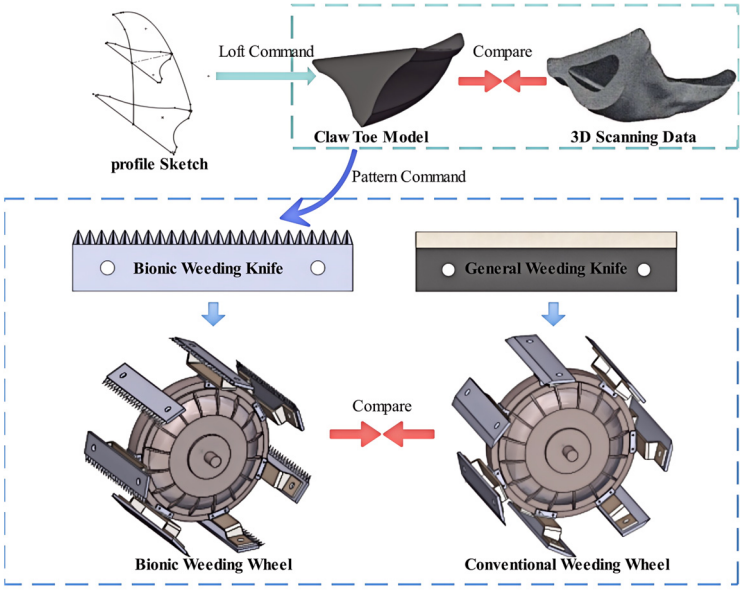


Figure 25. Schematic diagram of biomimetic weeding wheel modeling and comparison.

Based on the single claw toe model, the overall integration design of the weeding tool was implemented in SolidWorks. The patterning tool was used to uniformly arrange the claw toe models on the tool base in a rake array, replicating the "multi-tooth collaborative

cutting" feature of mole cricket claws and ultimately forming a 3D model of the bionic weeding blade. In contrast to conventional weeding blades, where both the upper and lower shovel surfaces are flat, the teeth of the bionic blade exhibit bionic curved surface characteristics. Notably, the two types of blades share identical dimensional parameters, with the only difference being their surface geometric profiles. Subsequently, the blades were circumferentially arranged around the hub motor to construct the weeding wheel mechanism. A comparison of the bionic and conventional weeding wheels is shown in Figure 26. This bionic design transitions from simulating a single biological feature to developing an engineering tool system, providing a foundational basis for subsequent cutting performance analysis.

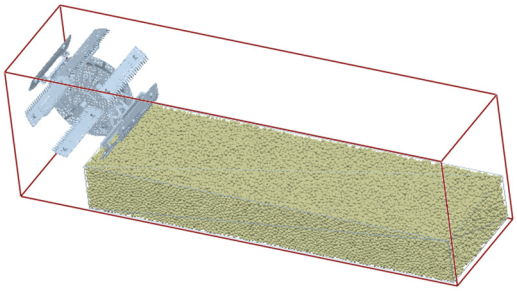


Figure 26. Diagram of simulation environment construction.

4. Discrete Element Method (DEM)-Based Simulation Analysis

4.1. Establishment of the Discrete Element Model

Two 3D models of the weeding wheel were established in SolidWorks, sharing the same dimensional parameters but differing in blade design. Both models were exported in STP format and imported into EDEM 2022 software, where a virtual soil tank with dimensions of 1000 mm × 400 mm × 150 mm was constructed, as shown in Figure 26. This study focuses on weeding during sesame seedlings' critical intertillage stage, when their roots are shallow, underdeveloped, and fragile—a weeding depth exceeding 3 cm would easily damage the roots and hinder seedling growth, while 3 cm can effectively remove weeds (mostly concentrated in the 0–3 cm topsoil during intertillage) and avoid root injury [25,26]. Thus, the soil penetration depth of both models was uniformly set to 3 cm, selected as the core simulation parameter to verify the model's reliability and the device's weeding performance.

The fundamental principle of EDEM-based discrete element method (DEM) simulation is to model soil particles as spheres. Currently, most researchers adopt spheres with a diameter of less than 10 mm for soil modeling [27–29]. During the simulation, the size and quantity of soil particles affect both simulation duration and accuracy: larger particle sizes and greater quantities improve simulation result accuracy, but also significantly extend the simulation time. After careful consideration, a soil particle radius of 5 mm was selected. Based on previous experimental results and relevant literature data, the property parameters and contact parameters of the soil and weeding blades (made of 65Mn steel) were configured [30,31], as presented in Table 6.

This simulation study on sesame in-row soil-penetrating weeding in the Huang-Huai region employed the Hertz-Mindlin with Bonding contact model in EDEM software. Excelling in simulating complex soil particle interactions, this model effectively captures inter-particle bonding mechanisms, thereby enabling accurate modeling of liquid bridge forces between soil particles [32,33].

Field measurements in sesame cultivation areas showed that, for the 0–10 cm soil layer, the actual moisture content ranged from 16% to 18%, the soil density was approximately

1850 kg/m^3, and the average particle radius was 5 mm. Given that soil moisture content significantly influences particle cohesion characteristics in this region, a moisture content (W) of 17% was adopted for the 0–10 cm soil layer to align with field practical conditions. Under these parameters, precise calculation of the particle cohesion radius is essential. Based on relevant theoretical frameworks, the derivation was conducted using the following formula [34]:

$$W = \frac{m_1}{(m_1 + m_2)} = \frac{\rho_2 v_2}{\rho_1 v_1 + \rho_2 v_2} \quad (17)$$

$$v_1 = \frac{4}{3}\pi R_1^3 \quad (18)$$

$$v_2 = \frac{4}{3}\pi R_2^3 - \frac{4}{3}\pi R_1^3 \quad (19)$$

In the formula, ρ_1—Soil density, kg/m^3.
ρ_2—Density of water, kg/m^3.
m_1—Mass of soil particles, kg.
m_2—Mass of moisture, kg.
v_1—Volume occupied by soil, m^3.
v_2—Volume occupied by moisture, m^3.
R_1—Soil particle radius, mm.
R_2—Soil cohesion radius, mm.

Table 6. Particle and Material Property Parameters.

Project	Parameter Values
Soil Poisson ratio	0.35
Soil shear modulus (Pa)	1×10^6
Soil density (kg/m^3)	1850
65Mn Poisson ratio	0.288
65Mn shear modulus (Pa)	7.6×10^{10}
65Mn density (kg/m^3)	7820
Soil particle–soil particle elasticity recovery factor	0.2
Soil particle–soil particle static friction coefficient	0.5
Soil particle–soil particle kinetic friction coefficient	0.3
Soil particle–65Mn elasticity recovery factor	0.3
Soil particle–65Mn static friction coefficient	0.5
Soil particle–65Mn kinetic friction coefficient	0.05

By solving the formulas simultaneously, the soil cohesion radius under the set conditions in the Huang-Huai region was calculated to be approximately 5.57 mm, and rounded to 5.6 mm. This value provides practical parameters for simulating the soil mechanical behavior during sesame field weeding via the Hertz-Mindlin with Bonding model, enhancing the accuracy of the weeding device's performance simulation. Specific model parameter settings are shown in Table 7 [35].

Table 7. Particle Contact Model Parameters.

Project	Parameter Values
Legal stiffness/(N·m^{-3})	5×10^7
Tangential stiffness/(N·m^{-3})	5×10^7
Critical normal stress/Pa	30,000
Tangential normal stress/Pa	30,000
Adhesion radius/mm	5.6

4.2. Simulation Test Design and Indicators

The operating torque (reflecting the tool's soil penetration resistance) and soil disturbance rate (reflecting weeding effectiveness) are used as core evaluation indicators for the operational performance of the bionic weeding wheel.

Operating torque data were collected using the mechanical monitoring function in EDEM's post-processing module. In the simulation model, the weeding wheel was set to rotate at 3 r/s around the *Y*-axis, with a linear travel speed of 0.3 m/s along the *X*-axis and a soil penetration depth of 3 cm. A mechanical sensor captured the instantaneous torque of the rotating shaft in real time at a sampling interval of 0.1 s. Torque time-series data from 1 to 3 s were exported for subsequent analysis.

The soil disturbance rate is defined as the ratio of displaced soil volume to the total soil volume within the tillage width of the weeding wheel. During EDEM post-processing, a 1500 × 400 × 500 mm collection box was constructed above the soil particles to capture displaced particles, as shown in Figure 27. A detection zone was delineated, with its length matching the travel distance of the weeding blades, width corresponding to the working width, and height equal to the soil penetration depth. The total number of particles within this zone was counted. After 3 s of simulation, the disturbance rate was calculated as the ratio of particles collected in the box to the total number of particles in the detection zone.

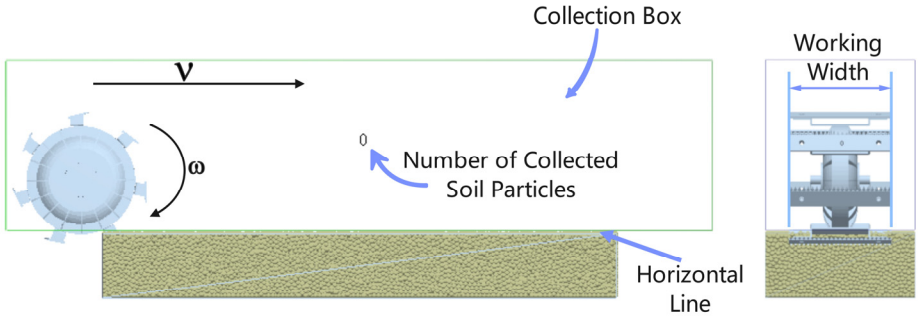


Figure 27. Schematic diagram of the soil particle collection box.

4.3. Analysis of Simulation Results

4.3.1. Torque Performance Analysis

The torque variations in the bionic weeding wheel and conventional weeding wheel during 1–3 s simulated motion are shown in Figure 28, which presents the total torque and X, Y, Z axis torque characteristics of the two weeding wheels, providing reference for tool performance analysis and optimization.

Simulation tests showed that the forces acting on the weeding components exhibited periodic fluctuations, with both the three-axis torques (X, Y, Z axes) and the total torque following this pattern. These fluctuations arose from the unbalanced forces on both sides of the weeding components during operation, generating fluctuating torques along the X and Z axes. Excessive fluctuations can induce cutter shaft vibration and tool chatter, accelerating component damage and fatigue. The torque about the *Y*-axis is of similar magnitude to the total torque but opposite in direction to the cutter shaft rotation. It serves to balance the torque of the transmission shaft. At a constant rotational speed, the magnitude of the *Y*-axis torque directly reflects the soil penetration resistance and power consumption: higher torque indicates greater resistance and energy consumption.

A comparative analysis revealed that the torque fluctuation amplitudes of the bionic weeding wheel along the X and Z axes were significantly smaller than those of the conventional weeding wheel, indicating more balanced forces on both sides during soil cutting. This reduced fluctuating torques, mitigated the risks of cutter shaft vibration and component fatigue, and enhanced operational stability. Regarding the *Y*-axis torque, the average

value for the bionic weeding wheel over 1–3 s was 7.75 N·m, representing a 17.4% reduction compared to the conventional weeding wheel (9.38 N·m). This indicates that the bionic weeding wheel exhibited lower soil penetration resistance and power consumption at the same rotational speed, thereby reducing energy waste while maintaining weeding quality and improving operational efficiency. The DEM model was validated via field experiments using the same operational parameters as the simulation (rotational speed: 3 r/s, travel speed: 0.3 m/s, weeding depth: 3 cm). A PXC-D20A power meter (voltage range: 6–200 V, maximum current: 20 A, accuracy: ±0.5%) was used to measure the actual average power (P) of conventional and bionic weeding wheels. Measured power data were exported, and real-time torque was calculated with the formula $T = \frac{9550 \cdot P}{n}$, where T denotes the torque in N·m, P represents the power in kW, and n is the rotational speed in r/min. Results showed a 3.8% relative error between simulated and experimental values, verifying the high reliability of the developed DEM model.

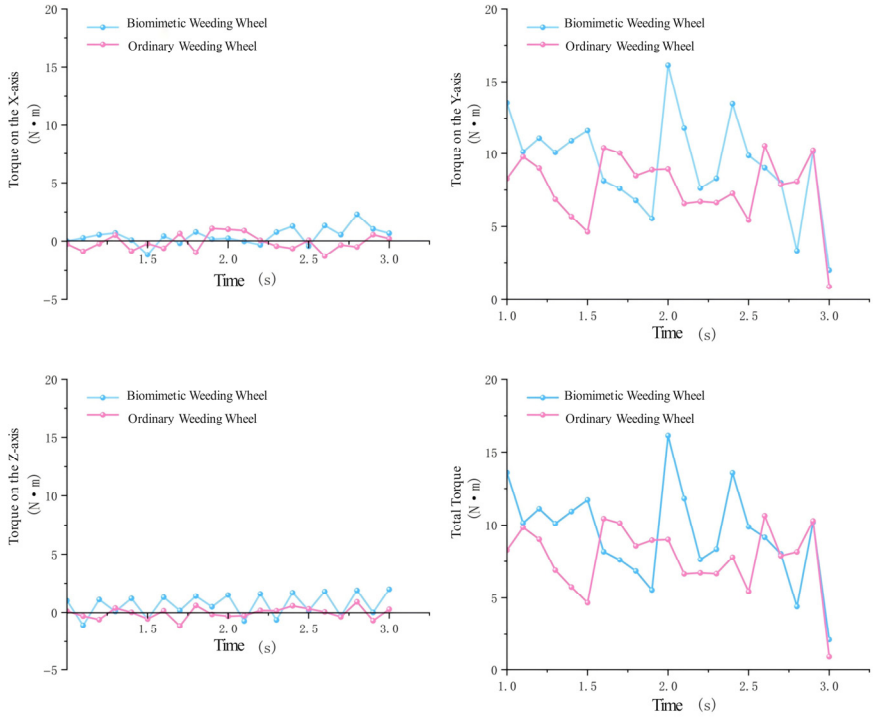


Figure 28. Diagram of torque variation.

4.3.2. Soil Disturbance Rate Analysis

The basic parameters for the simulation tests were set as follows: the operating width of the weeding wheel was 24 cm, the travel distance within 3 s was approximately 90 cm, the operating depth was 3 cm, the soil particle radius was 5 mm, and the total number of soil particles within the tillage width was 6560, as shown in Figure 29.

The simulation results indicated that, after 3 s of operation, the bionic weeding wheel displaced 6246 soil particles, corresponding to a soil disturbance rate of approximately 95.2%, as shown in Figure 30a. In comparison, the conventional weeding wheel displaced 5710 particles during the same period, with a soil disturbance rate of approximately 87.0%, as shown in Figure 30b. The soil disturbance rate of the bionic weeding wheel was 8.2 percentage points higher than that of the conventional one, demonstrating a significant advantage. This indicates that the morphological design of the bionic blade teeth enables more efficient soil penetration and force transmission, displacing more soil particles within the tillage width. The DEM model was validated via field experiments using the same simulation parameters (rotational speed: 3 r/s, travel speed: 0.3 m/s, weeding depth: 3 cm).

The weeding rates of the conventional and bionic weeding wheels were determined by counting the number of residual weeds in the test plots before and after the operation and calculating the weed removal ratio. The results showed that the weeding rate of the bionic weeding wheel was 9.1% higher than that of the conventional one, which confirmed the high reliability of the established DEM model.

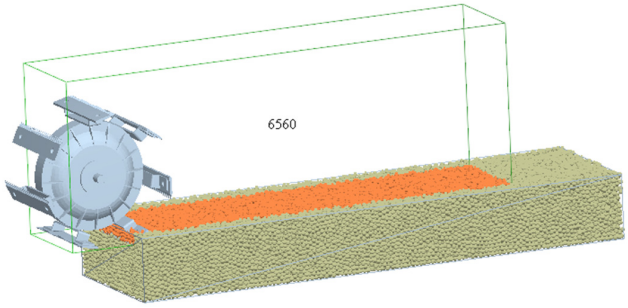


Figure 29. Diagram of the total number of soil particles within the tillage width.

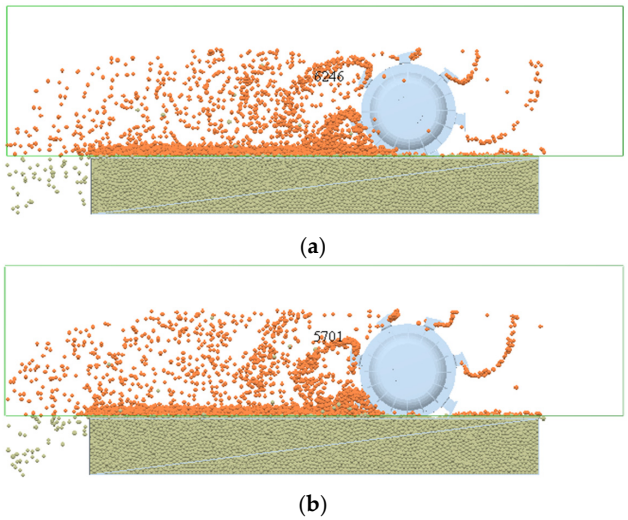


Figure 30. Comparison diagram of the number of disturbed soil particles: (**a**) schematic diagram of simulation results of biomimetic weeding wheel; (**b**) schematic diagram of simulation results of Conventional Weeding Wheel.

4.3.3. Soil Particle Motion Behavior Analysis

During the operation of the weeding wheel, the impact and cutting action of the weeding blade cause the surface soil to be disturbed and lifted upward, completing the soil penetration and weeding process. The biomimetic weeding wheel exhibits different soil interaction patterns compared to conventional models due to structural differences (as illustrated in Figure 31).

A comparative analysis of soil particle velocity distribution revealed that the high- and low-velocity particles (light color for high velocity, dark color for low velocity) of the bionic weeding wheel remained relatively orderly at different time points. The average velocity of soil particles within the collection box above the soil was 0.52 m/s within 1–2.5 s, indicating that, influenced by the bionic structure, the velocity transmission and variation in soil particles were more regular. The breakage of bonding forces and velocity acquisition were more rhythmic, and the soil disturbance and lifting actions were more coherent. In contrast, the conventional weeding wheel exhibited weak "layered characteristics" in its particle velocity distribution, with obvious mixing of high- and low-velocity particles and poor orderliness in velocity transmission. Its average velocity reached 0.58 m/s within 1–2.5 s, accompanied by continuous and severe soil splashing.

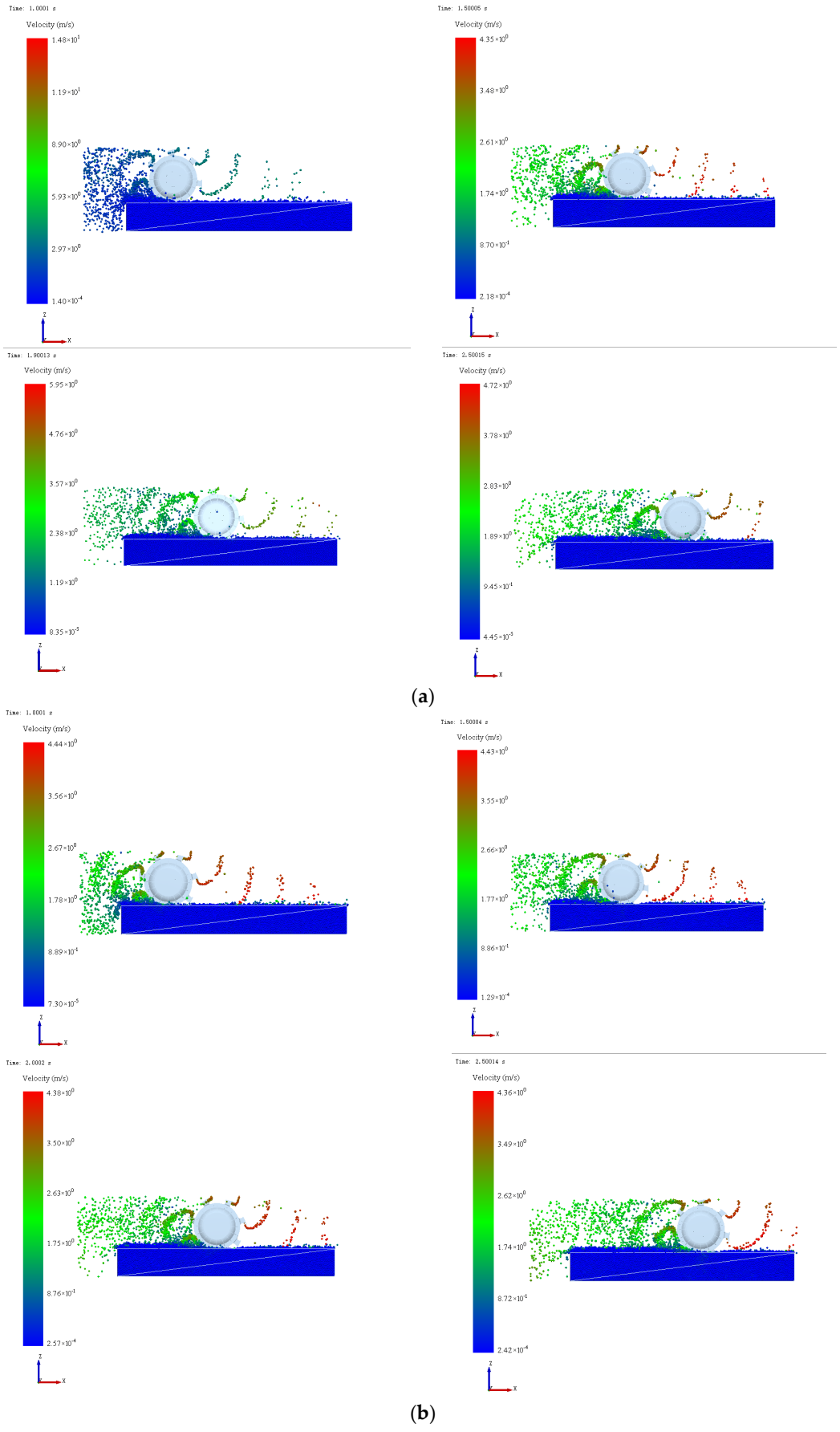


Figure 31. Diagram of Soil Particle Motion States: (**a**) soil movement process of biomimetic weeding wheel; (**b**) soil movement process of ordinary weeding wheel.

A comparison of soil throwing and adhesion showed that the bionic weeding wheel produced a concentrated backward soil flow. The amount of soil adhering to the blades and being thrown forward after one rotation was minimal and controllable. This enables predictable soil trajectories, effective weeding through soil throwing, reduced adhesion interference, and a high effective operation ratio during penetration. In contrast, the conventional weeding wheel exhibited disorganized soil throwing and adhesion, with scattered backward soil, unstable post-adhesion throwing, weak movement control, ineffective work consumption, and lower accuracy and efficiency. These issues were attributed to poor soil movement regulation and potential weeding continuity problems.

In summary, the bionic weeding wheel outperforms the conventional one in soil particle velocity regulation and throwing control, enabling more orderly and efficient soil disturbance. This highlights the advantages of bionic design in optimizing soil-blade interaction, whereas the conventional weeding wheel lacks such motion control capabilities.

5. Conclusions

1. Advantages of the Integrated System: The vehicle adopts a modular structure for three-row weeding and four-row plant protection, coupled with an extended-range hybrid powertrain. Its parallel linkage design allows vertical self-adaptation to uneven terrain, ensuring a consistent weeding depth of 3–6 cm and stable spraying height. Combined with an adjustable spraying width and a closed-loop "detection–feedback–adjustment" mechanism to avoid collisions with sesame plants, the vehicle is fully adaptable to the agronomic requirements of narrow-row cultivation.

2. Bionic Design Innovation: Inspired by mole cricket forelegs, the bionic weeding wheel integrates quantified biological features—quadratically fitted claw toe contours ($R^2 > 0.97$) and key morphological ratios (toe base height-width 1:2, toe groove radius-toe height 1:1). This addresses the drag and penetration limitations of conventional flat blades, realizing a reliable biological-to-engineering design transformation.

3. DEM-Validated Performance: EDEM simulations confirm the bionic wheel outperforms conventional designs: 17.4% lower average torque (7.75 N·m vs. 9.38 N·m), 8.2-percentage-point higher soil disturbance rate (95.2% vs. 87.0%), and more ordered soil particle motion (2.98 m/s vs. 4.4 m/s average max velocity), reducing energy waste and improving weeding efficiency.

4. Application Value and Future Work: The vehicle meets the precision and efficiency requirements of sesame management, providing a scalable technical reference for narrow-row crop mechanization. Future research will focus on three directions: first, conducting field validation in the Huanghuai region to measure key indicators including actual energy consumption, weeding rate, crop damage rate, and droplet distribution uniformity, and determining the optimal operating parameters of the vehicle (e.g., rotational speed, forward speed, and weeding height) through orthogonal experiments based on these indicators; second, exploring the optimal operating parameters under different soil conditions and moisture gradients; third, extending compatibility to other narrow-row crops (rapeseed, millet) and developing an intelligent control system for adaptive parameter regulation based on real-time soil moisture and weed density detection.

Author Contributions: Conceptualization, D.G.; Methodology, D.G.; Software, J.Z.; Validation, J.Z.; Formal analysis, Y.W.; Investigation, Y.W.; Resources, J.Y.; Data curation, X.Z.; writing—original draft preparation, D.G.; writing—review and editing, X.Z.; Visualization, X.X.; Supervision, H.S.; Project administration, J.Y.; Funding acquisition, D.G. All authors have read and agreed to the published version of the manuscript.

Funding: Science and Technology Research and Development Special Project of Henan Province (grant number 2321021111131). National Natural Science Foundation of China (grant number 32401692). Henan Province Science and Technology Research Project (grant number 242102110336). Key Research Programs of Higher Education Institutions in Henan Province (grant number 25B416001).

Institutional Review Board Statement: Not applicable.

Informed Consent Statement: Not applicable.

Data Availability Statement: The data presented in this study are available upon request from the Corresponding author. The data are not publicly available due to privacy concerns.

Conflicts of Interest: The authors declare that the research was conducted in the absence of any commercial or financial relationships that could be construed as a potential conflict of interest.

References

1. You, J.; Guo, Y.Z.; Zhao, Y.Z.; Wang, L.H. Distribution, Origin and Domestication of Cultivated Sesame. *Chin. J. Oil Crop Sci.* **2024**, *46*, 959–968. [CrossRef]
2. Qin, L.L.; Miao, H.M.; Zhang, Z.Y.; Duan, Y.H.; Zhang, H.Y. Analysis of World Sesame Production Status and Development Trends. *China Oils Fats* **2023**, *49*, 1–9. [CrossRef]
3. Sha, H.; Huang, Q.X.; Lei, Z.H.; Zhang, L.; Xiang, L.J. Key Techniques for Sesame Cultivation. *Rural Sci. Technol.* **2023**, *1*, 14–17. [CrossRef]
4. Zhao, L.; Wang, Q.; Xu, G.Z.; Wu, Y.H.; Yin, E.; Chen, P. Current Situation, Low-Yield Causes and High-Yield Cultivation Techniques of Sesame in Jianghuai Region. *J. Anhui Agric. Sci.* **2010**, *38*, 12397–12399.
5. Qiao, Z.Y.; Meng, K. Dynamics and Control Measures of Rice Weeds in Gongqing Farm, Heilongjiang Province. Master's Thesis, Heilongjiang University, Harbin, China, 2013.
6. Li, D.S.; Zhang, L.J.; Gai, Z.W. Research Status of Weeding Technology at Home and Abroad. *For. Eng.* **2019**, *18*, 17–18.
7. Jiang, T.D.; Ouyang, A.G. Agricultural Machinery Intellectualization and 21st Century Precision Agriculture. *Agric. Mach. Res.* **2018**, *40*, 12–15.
8. Lu, Y.X. Scientific Significance and Frontiers of Bionics: Significance and Development of Bionics. *Sci. Chin.* **2014**, *4*, 22–24.
9. Sivesind, E.C.; LeBlanc, M.L.; Cloutier, D.C.; Seguin, P.; Stewart, K.A. Impact of Selective Flame Weeding on Onion Yield, Pungency, Flavonoid Concentration, and Weeds. *Crop Prot.* **2017**, *39*, 45–51. [CrossRef]
10. Maciejewski, J.; Jarzebowski, A.; Trampczynski, W. Study on the Efficiency of the Digging Process Using the Model of Excavator Bucket. *J. Terramech.* **2019**, *40*, 221–233. [CrossRef]
11. Fernandez, J.E. Materials Selection to Excavator Teeth in Mining Industry. *Wear* **2019**, *250*, 11–18. [CrossRef]
12. Maciejewski, J.; Jarzebowski, A. Optimisation of Tool Trajectory in Soil Digging Processes—Laboratory Tests. *J. Terramech.* **2015**, *39*, 161–179. [CrossRef]
13. Coetzee, C.J.; Els, D.N.J. Calibration of Discrete Element Parameters and the Modeling of Silo Discharge and Bucket Filling. *Comput. Electron. Agric.* **2009**, *65*, 198–212. [CrossRef]
14. Ma, X.R.; Zhuang, W.D. Research Progress and Analysis of Intelligent Weeder Technology. *Mod. Agric.* **2025**, *5*, 91–93.
15. Li, S.Z.; Wang, L.J. Investigation on the Application of Mechanical Weeding Technology and Equipment and Development Suggestions. *Agric. Eng.* **2024**, *14*, 19–22.
16. Gonzalez-De-Soto, M.; Emmi, L.; Perez-Ruiz, M.; Aguera, J.; Gonzalez-de-Santos, P. Autonomous Systems for Precise Spraying—Evaluation of a Robotised Patch Sprayer. *Biosyst. Eng.* **2016**, *146*, 165–182. [CrossRef]
17. Zhang, D.; Huang, H.; Ren, L.Q. Soil Cutting Test and Drag Reduction Mechanism of Bionic Bucket Teeth for Excavators. *Trans. Chin. Soc. Agric. Mach.* **2013**, *32*, 120–121. [CrossRef]
18. Chen, H.Y.; Zhuang, W.D. Research Status and Development Analysis of Intelligent Weeding Machinery. *Mod. Agric.* **2025**, *2*, 91–93.
19. Huang, W.M. Research Status and Operation Mode Selection of Mechanical Weeding Technology. *Agric. Eng.* **2024**, *14*, 10–13. [CrossRef]
20. Tian, H.L.; Xie, F.X.; Yan, X.L.; Wang, F.X.; Zhang, W.Q.; Liu, Y. Key Technologies and Application of Whole-Process Mechanized Sesame Production. *Heilongjiang Agric. Sci.* **2025**, *5*, 114–119.
21. Zhang, W.M.; Sun, Y.; Li, W.F.; Liu, J.Q.; Wu, Z.H. Occurrence Regularity and Control Techniques of Major Sesame Diseases in Huanghuai Region. *Agric. Sci. Technol. Commun.* **2024**, *6*, 191–192. [CrossRef]
22. Zhang, Y. Study on Biocoupling Characteristics of Mole Cricket's Soil-Contacting Parts. Master's Thesis, Jilin University, Changchun, China, 2008.

23. Li, C.M. Design and Analysis of a Bionic Mole Cricket Peanut Digging Shovel. Master's Thesis, Shenyang Agricultural University, Shenyang, China, 2018.
24. Zhang, Y.; Qiao, C.X.; Wang, T.Q.; Cao, J.; Wang, P.; Shi, L. Drag Reduction Mechanism of the Three-Dimensional Geometric Configuration of Mole Cricket Foreleg Claw Toes. *Trans. Chin. Soc. Agric. Eng.* **2021**, *37*, 309–315. [CrossRef]
25. Zhou, Z. Sesame Cultivation Technology. *Henan Agric.* **2020**, *28*, 19–20.
26. Chen, H. Cultivation and Management Measures for Sesame Seedling Stage. *Henan Agric.* **2022**, *22*, 45.
27. Ucgul, M.; Fielke, J.M.; Chris, S. 3D DEM Tillage Simulation: Validation of a Hysteretic Spring (Plastic) Contact Model for a Sweep Tool Operation in a Cohesionless Soil. *Soil Tillage Res.* **2014**, *144*, 220–227. [CrossRef]
28. Chen, Y.; Lars, J.M.; Tavs, N. A Discrete Element Model for Soil-Sweep Interaction in Three Different Soils. *Soil Tillage Res.* **2013**, *126*, 34–41. [CrossRef]
29. Wang, X.L.; Hu, H.; Wang, Q.J.; Li, H.; He, J.; Chen, W. Parameter Calibration Method of Soil Model Based on Discrete Element Method. *Trans. Chin. Soc. Agric. Mach.* **2017**, *48*, 78–85. [CrossRef]
30. Xiao, M.H.; Wang, K.X.; Yang, W.; Wang, W.; Jiang, F. Design and Experiment of Bionic Rotary Tiller Based on Claw Toes of Oriental Mole Cricket. *Trans. Chin. Soc. Agric. Mach.* **2021**, *52*, 55–63.
31. Liu, K.Y.; Su, H.J.; Li, F.Y.; Jiao, W. Parameter Calibration of Soil Discrete Element Model Based on Response Surface Methodology. *Chin. J. Agric. Mach.* **2021**, *42*, 143–149.
32. Zhu, Y.H.; Xia, J.F.; Zeng, R.; Zheng, K.; Du, J.; Liu, Z. Research on Rotary Tilling Power Consumption Prediction Model for Paddy Field Based on Discrete Element Method. *Trans. Chin. Soc. Agric. Mach.* **2020**, *51*, 42–50.
33. Potyondy, D.O.; Cundall, P.A. A Bonded-Particle Model for Rock. *Int. J. Rock Mech. Min. Sci.* **2004**, *41*, 1329–1364. [CrossRef]
34. Zhao, J.G.; Zhao, C.F.; Li, H.; Qi, H.K.; Ma, Y.J.; Lu, Z.X. Design and Experiment of Corn Liquid Topdressing and Weeding Machine. *J. Hebei Agric. Univ.* **2022**, *45*, 130–138.
35. Ma, Y.; Wang, A.; Zhao, J.; Hao, J.; Li, J.; Ma, L.; Zhao, W.; Wu, Y. Simulation Analysis and Experiment on Drag Reduction Effect of Convex Round-Edge Subsoiler Based on Discrete Element Method. *Trans. Chin. Soc. Agric. Eng.* **2019**, *35*, 16–23. [CrossRef]

Disclaimer/Publisher's Note: The statements, opinions and data contained in all publications are solely those of the individual author(s) and contributor(s) and not of MDPI and/or the editor(s). MDPI and/or the editor(s) disclaim responsibility for any injury to people or property resulting from any ideas, methods, instructions or products referred to in the content.